

## RESEARCH ARTICLE

# Wind turbine boundary layer arrays for Cartesian and staggered configurations: Part II, low-dimensional representations via the proper orthogonal decomposition

Nicholas Hamilton<sup>1</sup>, Murat Tutkun<sup>2,3</sup> and Raúl Bayoán Cal<sup>1</sup>

<sup>1</sup> Department of Mechanical and Materials Engineering, Portland State University, Portland, Oregon 97201, USA

<sup>2</sup> Department of Process and Fluid Flow Technology, Institute for Energy Technology, PO Box 40, 2027 Kjeller, Norway

<sup>3</sup> École Centrale de Lille, Université Lille Nord de France, 59655 Villeneuve d'Ascq, France

## ABSTRACT

Cartesian and row-offset wind turbine array configurations were tested investigating the wake interaction and recovery dynamics. The snapshot proper orthogonal decomposition is applied to velocity measurements. Resulting modes are used in constructing low-dimensional descriptions of turbulence statistics including the turbulence kinetic energy production and the flux of turbulence kinetic energy. Descriptions of the turbulent behavior are made on the basis of the span of the streamwise average profile of the Reynolds shear stress,  $-\bar{u}\bar{v}$ , with the addition of orthogonal modes. The Reynolds stress criterion was selected for the convergence of the model as it is a good representation of the range of turbulent dynamics in the wake of a wind turbine. The description demonstrates that the turbulence kinetic energy production and the flux of turbulence kinetic energy are accurately rebuilt with approximately 1% of the total resultant orthogonal modes. Structures associated with the top-tip of the rotor blade reconstruct with fewer modes than those associated with the bottom-tip of the rotor or the nacelle. This confirms that the greatest part of the turbulence kinetic energy is located high in the turbine canopy as described by the turbulent stresses. Overall, behavior of individual turbines in recovered positions within the arrays requires fewer modes to converge than those in locations with less recovered inflows. Copyright © 2014 John Wiley & Sons, Ltd.

## KEYWORDS

atmospheric boundary layer; wind turbine array; wake recovery; turbulence; production; flux of kinetic energy; snapshot POD; low-dimensional model

## Correspondence

Raúl Bayoán Cal, Department of Mechanical and Materials Engineering, Portland State University, Portland, Oregon 97201, USA.  
E-mail: cal@me.pdx.edu

Received 15 April 2013; Revised 7 January 2014; Accepted 8 January 2014

## 1. INTRODUCTION

The proper orthogonal decomposition (POD) has proven to be an effective means of identifying energetic structures in turbulent flows.<sup>1–4</sup> Further, because POD organizes the structures within turbulence according to energy content, low-dimensional descriptions based on fewer degrees of freedom can be used to reconstruct flow statistics omitting the energy associated with high frequency motions or small scales.<sup>5</sup> Performing POD analysis to data results in a set of ordered modes that correspond to the energy containing events in a flow field. POD can only be applied to multipoint measurements including rakes of hot-wire probes, usually carried out in the *classical* POD, or scalar visualization data, particle image velocimetry (PIV), or data resulting from numerical simulations, all of which are typically carried out in the form of *snapshot* POD. Berkooz *et al.*<sup>2</sup> provide a comprehensive survey of the early applications.

The POD is limited in its ability to organize structures, events or patterns by the nature of input data as inherently stochastic as noted in the study by Bonnet *et al.*<sup>6</sup> The analysis may also associate infrequent events with higher mode numbers because they are not coherent or do not carry much energy in a statistical sense, regardless of their dynamical

importance.<sup>4</sup> The POD applied to random data showing homogeneous behavior in any particular dimension or direction reduces to a Fourier decomposition.<sup>7</sup> In such a case, Fourier transformation is the only applicable decomposition but leads to a limited description of local flow structures and must retain a large number of modes to describe the dynamics of the flow.<sup>8</sup> Because these processes lead to a mixture of Fourier and POD modes, it becomes more difficult to identify the characteristic behavior or shape of structures.

Axisymmetric far-wakes have been investigated via the POD in the study by Tutkun *et al.*,<sup>9</sup> in which many separate applications of the POD were applied to experimental hot-wire data to determine the dependence of rate of energy accumulation by POD modes on components of velocity. The accumulation of energy was tested for individual components of velocity in a scalar sense, two-component and three-component vectorial POD schemes were also tested and compared with the sum of modal energy content of scalar POD applications. In most applications of the POD to turbulent flow data, the inclusion or exclusion of any particular component of velocity data does not greatly affect the distribution of energy content in the range of modes, provided that the dominant velocity component is included in construction of the kernel. In the study of the axisymmetric far-wake, peaks of energy described by the eigenvalues of the POD were more easily distinguished by excluding selected velocity components, although the energy described by the eigenvalues did not change drastically.

The POD has been applied to multipoint field measurements spanning the rotor area in front of a wind turbine.<sup>10</sup> The results were used to formulate a low-dimensional representation of the inflow and subsequently fed into fatigue and loading simulations for the rotor blades. The result of this application addressed the effects of large-scale turbulence on the loading and life cycles of a turbine. Because the outflow of the turbine was not investigated, no correlations were made between the energetic POD modes and the power output of the turbine. The spanwise and vertical components of inflow velocity were omitted from the POD on the assumption that they were already in their principle components. Reconstructions of up to the first five modes were used in the bending fatigue load simulations.

Identifying the turbulent wake structures influencing the performance of turbines in an array is followed in the present research. It is currently understood that the large structures are responsible for a majority contribution to wake recovery by the entrainment of kinetic energy from above the turbine canopy. An experiment was designed at Portland State University to test the performance of wind turbine models in various configurations within an array. Coupled with measurements of power output are flow measurements in the form of stereo-PIV (SPIV). Energy containing structures are distinguished and analyzed using snapshot POD, and reconstructions of the flow and quantities including the flux of kinetic energy are made on the basis of a finite number of POD modes. Analysis of the flow field and power measurements as well as the characteristics of the experiments is provided in the first part of this paper.

## 2. THEORY

The formulation of an orthonormal vector basis from random data was used in many applications such as principle component analysis (as early as 1901) and singular value decomposition before the theory was applied to flow measurements. The POD was introduced to the realm of fluid mechanics as a means of analysis by Lumley.<sup>11</sup> A derivation of the classical POD can be found in the study by Lumley as well as Pedersen.<sup>7,11,12</sup> Since the focus of this work lies on the snapshot POD, the theory for the classical POD has been omitted.

Following the notation of Pedersen<sup>12</sup> the method of snapshots, referred to from here as *snapshot* POD, is built on a basis of uncorrelated flow measurements. The snapshot POD is applied because field measurements, such as those obtained using PIV, typically contain the necessary spatial resolution, but lack temporal resolution. The snapshot POD was introduced by Sirovich<sup>13</sup> and is applied to scalar visual data with the intent to distinguish energetic structures on which flow fields are built. In the following development, bold math symbols represent vectorial quantities, whereas symbols in plain text are scalar quantities. The stochastic flow field can be written as,

$$\mathbf{u}_n = \mathbf{u}(\mathbf{x}, t^n) = \mathbf{u}(\mathbf{x}, n\tau), \quad n \in [1, \dots, N] \quad (1)$$

where  $\mathbf{x}$  and  $t^n$  refer to the spatial coordinates and time at sample  $n$ , respectively, and  $\tau$  is the time separation between measurements. The total number of snapshots above is described as  $N$ . The time separation,  $\tau$ , is typically at least twice the integral time scale to ensure that snapshots remain uncorrelated. With a large number of snapshots, the two-point spatial correlation tensor may be approximated as,

$$\mathbf{R}(\mathbf{x}, \mathbf{x}') = \frac{1}{N} \sum_{n=1}^N \mathbf{u}(\mathbf{x}, t^n) \mathbf{u}^T(\mathbf{x}', t^n), \quad (2)$$

where  $N$  denotes the number of snapshots and the prime represents the spatial coordinate of another point in the domain.

The two-point spatial correlation tensor becomes the kernel of the POD eigenvalue problem solved numerically. It is then assumed that a basis of  $N$  modes can be written in terms of the original data as,

$$\Phi(\mathbf{x}) = \sum_{i=1}^N A(t^i) \mathbf{u}(\mathbf{x}, t^i), \quad (3)$$

where  $\Phi(\mathbf{x})$  is a deterministic field that has the largest projection on the stochastic velocity field in a mean square sense.

The POD integral equation writes,

$$\int_{\Omega} \mathbf{R}(\mathbf{x}, \mathbf{x}') \Phi(\mathbf{x}') d\mathbf{x}' = \lambda \Phi(\mathbf{x}). \quad (4)$$

Substituting equations (2) and (3) into equation (4) and discretizing in order to solve the integral equation numerically yields an eigenvalue problem in the following form:

$$\mathbf{CA} = \lambda \mathbf{A}. \quad (5)$$

In equation (5), the coefficient vector is

$$\mathbf{N} = [A(t^1), A(t^2), \dots, A(t^n)]^T. \quad (6)$$

and the elements of the matrix  $\mathbf{C}$  are

$$C_{jk} = \frac{1}{N} (\mathbf{u}^T(\mathbf{x}, t^j) \mathbf{u}(\mathbf{x}, t^k)), \quad j, k = 1, \dots, N \quad (7)$$

Solving equation (5) yields the set of coefficients from which the POD modes are computed according to equation (3). These modes are typically normalized to form an orthonormal basis as

$$\Phi^i(\mathbf{x}) = \frac{\sum_{i=1}^N A^i(t^n) \mathbf{u}(\mathbf{x}, t^n)}{\|\sum_{i=1}^N A^i(t^n) \mathbf{u}(\mathbf{x}, t^n)\|}. \quad (8)$$

The stochastic velocity fields may then be reconstructed using the eigenfunctions of the POD,

$$\mathbf{u}(\mathbf{x}, t^n) = \sum_{n=1}^N a_n \Phi^n(\mathbf{x}), \quad (9)$$

where  $a_n$  is a set of coefficients obtained by back-projecting the set of stochastic velocity fields onto the deterministic POD modes,

$$a_n = \int_{\Omega} \mathbf{u}(\mathbf{x}, t^n) \Phi^n(\mathbf{x}) d\mathbf{x}'. \quad (10)$$

The two-point spatial correlation tensor,  $R_{ij}(\mathbf{x}, \mathbf{x}')$ , can also be reconstructed using the eigenfunctions and eigenvalues obtained through the POD.

$$R_{ij}(\mathbf{x}, \mathbf{x}') = \lambda_n \Phi_i^n(\mathbf{x}) \Phi_j^n(\mathbf{x}'). \quad (11)$$

By contraction of the reconstructed two-point spatial correlation tensor,  $R_{ij}(\mathbf{x}, \mathbf{x}')$ , the total turbulence kinetic energy,  $E$ , in the domain,  $\Omega$ , is equal to the summation of the eigenvalues,  $\lambda_n$ ,

$$E = \int_{\Omega} \overline{u_i(\mathbf{x}) u_i(\mathbf{x})} = \sum_{n=1}^N \lambda_n. \quad (12)$$

The overline denotes ensemble averaging of the given quantity.

Thus, the POD provides an optimal set of eigenfunctions that represents the modes of turbulence and eigenvalues that measure the energy associated with each eigenfunction. Fluctuating velocity measurements are reconstructed as in equation (9), and, as an extension, Reynolds stresses can be directly reconstructed as

$$\overline{u_i(\mathbf{x})u_j(\mathbf{x})} = \sum_{n=1}^N a_n \Phi_i^n(\mathbf{x})\Phi_j^n(\mathbf{x}). \quad (13)$$

The reconstructed Reynolds stresses in equation (13) are used to study different quantities in the transport equation for the mean kinetic energy. For this flow, the mean kinetic energy equation can be written as

$$U_j \frac{\partial \frac{1}{2} U_i^2}{\partial x_j} = -\frac{1}{\rho} U_i \frac{\partial P}{\partial x_i} + \overline{u_i u_j} \frac{\partial U_i}{\partial x_j} - \frac{\partial \overline{u_i u_j} U_i}{\partial x_j} - \mathcal{F}_{x_i}. \quad (14)$$

Balancing the convection are terms including the power added to the flow by a pressure gradient and the mechanical energy removed from the flow by the presence of the wind turbines,  $\mathcal{F}_{x_i}(\mathbf{x})$ , which acts primarily in the mean flow direction. The second and third terms on the right-hand side of the equation are the turbulence production,  $P_{ij}(\mathbf{x})$ , and flux of kinetic energy,  $F_{ij}(\mathbf{x})$ , respectively. In each of these terms, the turbulent stresses are represented well with POD reconstructions, whereas the mean velocity or respective gradient is taken from standard turbulence statistics.

### 3. EXPERIMENTAL SETUP

The snapshot POD detailed in Section 2 was applied to SPIV data collected in a wind tunnel experiment conducted at Portland State University. A full description of the experiment is found in *Part I* of the paper. For convenience, a brief description is outlined in the succeeding text. The experiment consisted of SPIV measurements taken directly upstream and downstream of entrance and exit row wind turbines in an array. Figure 1 provides an overview of the experimental arrangement. The boundary layer inflow is characterized in *Part I* of the paper. The effective friction velocity,  $u_*$ , velocity deficit,  $\Delta U^+$ , and effective surface roughness height,  $y_0$ , were obtained by a logarithmic fit in the constant shear layer of the inflow boundary layer. The inflow is conditioned through the addition of a passive grid and vertical strakes at the inlet of the tunnel as well as surface roughness upstream of the model wind turbine array. Wind turbine models were manufactured in-house and consisted of an electric motor for the nacelle and rotors formed out of bent sheet steel.

Measurements were made for different configurations of a wind turbine array shown in Figure 2. A  $4 \times 3$  Cartesian arrangement formed the base case to which two different row-offset configurations were compared. In each of the offset cases, alternating rows of turbines were given a spanwise shift of 1.5 rotor diameters such that non-leading turbines were directly between turbines of preceding rows in a spanwise sense. The (3 – 2 – 3 – 2) arrangement yielded an entrance row turbine whose particular inflow and dynamics are statistically identical to those of the base arrangement, and the (2 – 3 – 2 – 3) arrangement provided an empty position at the entrance row and an exit row turbine differing from that of the base arrangement. In Figure 2 and throughout the paper, the test cases are referred to with abbreviated titles. For the base arrangement, the entrance row turbine is base-center-front (BCF), and the exit row is base-center-back (BCB). For the row-offset arrangements, the entrance row is offset-center-front (OCF), and the exit row turbines are offset-center-1back (OC1) and offset-center-2back (OC2), respectively, for the first and second variations.

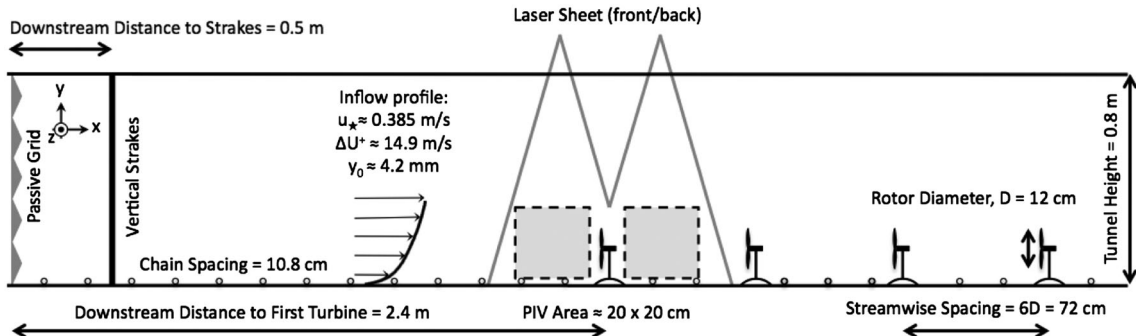


**Figure 1.** Schematic of experimental setup viewed from the user-side of the wind tunnel. The schematic above is for reference only; drawing is not to scale. Boundary layer characterization parameters are shown for reference.

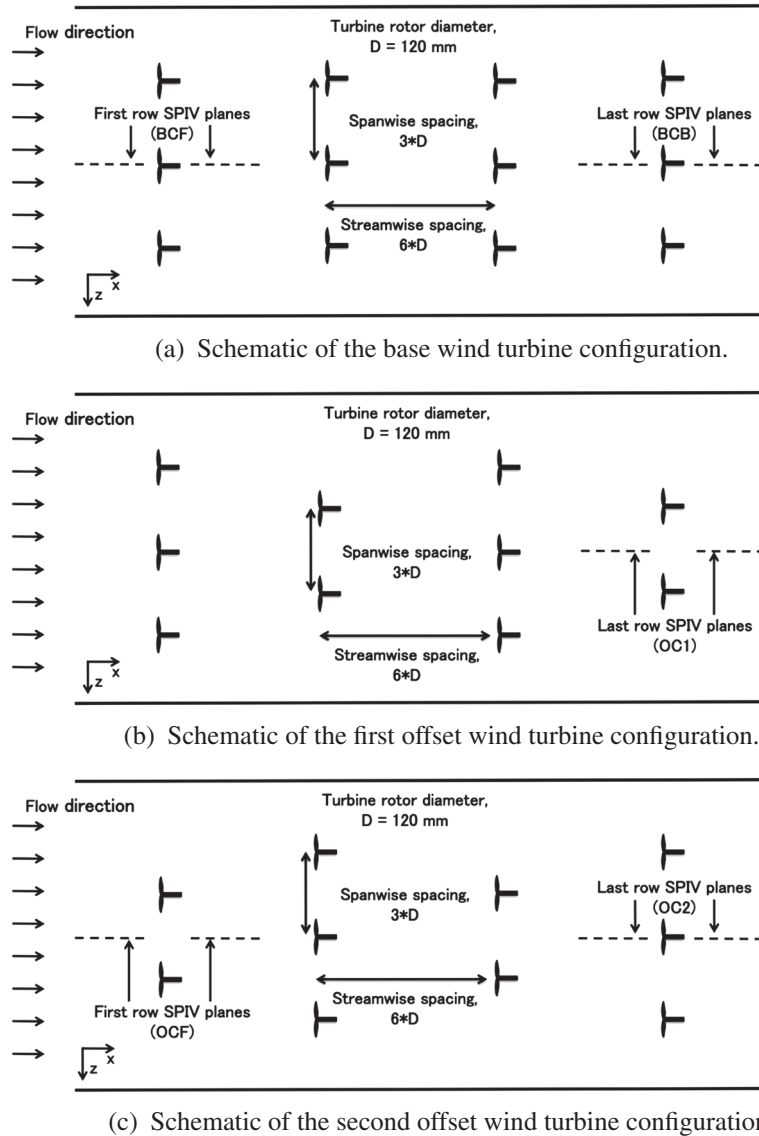


**Figure 2.** The streamwise spacing between rows,  $S_x$ , is six times the rotor diameter (0.72 m). The spanwise spacing between turbines,  $S_z$ , is three rotor diameters (0.36 m).

For all measurement cases, the wind tunnel was maintained at a constant speed such that the hub height velocity at the entrance row of turbine models was  $U_{hub} = 4.6 \text{ m s}^{-1}$ . The inflow boundary layer exhibited a friction velocity of  $u_* = 0.385 \text{ m s}^{-1}$ , an effective roughness of  $y_0 = 4.2 \text{ mm}$  and a momentum deficit of  $\Delta U^+ = 14.9 \text{ m s}^{-1}$ . In the area corresponding to the turbine rotors, the integral scale was about 0.12 m, and the turbulence intensity was approximately 15%. The Reynolds number, based on the diameter of the rotor ( $D$ ) and the hub height velocity ( $U_{hub}$ ), was  $3.7 \times 10^4$ . As detailed in the study by Chamorro *et al.*,<sup>14</sup> the main flow statistics for a wind turbine canopy layer becomes independent of Reynolds number in this range.

## 4. RESULTS

### 4.1. Turbulence statistics

Turbulence statistics are discussed at length in *Part I* of the paper. For convenience, a brief review of selected quantities is provided in the following text. Each of the quantities shown, in addition to the production of turbulence kinetic energy, are approached through the low-dimensional models described in subsequent results. In the contour plots of Figures 4 and

5, the windows correspond to positions directly upstream and downstream of wind turbine models in the array. Figure 3 shows the arrangement of contour plots in the following figures. As shown, the base configuration, the (3 – 2 – 3 – 2) and (2 – 3 – 2 – 3) row-offset configurations correspond to top, middle and bottom rows of the subfigures, respectively. The left pair of columns represent the entrance row of the arrays, and the right pair of columns correspond to the exit row. The entrance row of the (3 – 2 – 3 – 2) row-offset configuration has been omitted as it is statistically identical to that of the base arrangement.

The Reynolds shear stress  $-\bar{uv}$  is normalized with the square of the mean hub height velocity and is shown in Figure 4. Evidence of tip vortices can be seen in the very near wake of each turbine location in the proximity of the top-tip of the rotors ( $y/D \approx 1.5$ ). Tip vortex behavior is most clearly seen in the entrance row of the base arrangement and the exit row of the offset case (top-left and bottom-right pairs of subfigures, respectively). Recalling that the locations directly upstream of exit row turbines correspond to the far wake ( $4 < x/D < 6$ ) of the third row of turbines, one observes that the Reynolds stresses are persistent as inflow to non-leading row turbines.

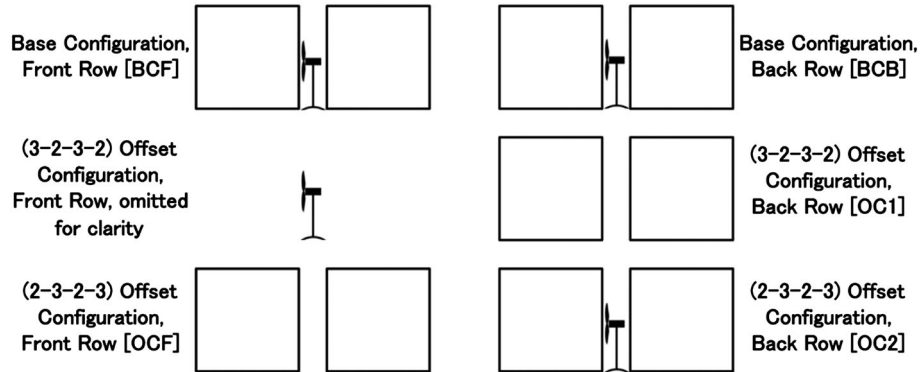


**Figure 3.** Measurement locations displayed in the following contour plots. Note that the data for the front row of the (3 – 2 – 3 – 2) offset configuration (center row) have been omitted as they are statistically identical to those of front row of the base configuration. The three measurement locations immediately upstream and downstream of wind turbines are marked with a turbine in the figure. Those without the turbine (OC1 and OCF) are empty positions within the offset arrays.

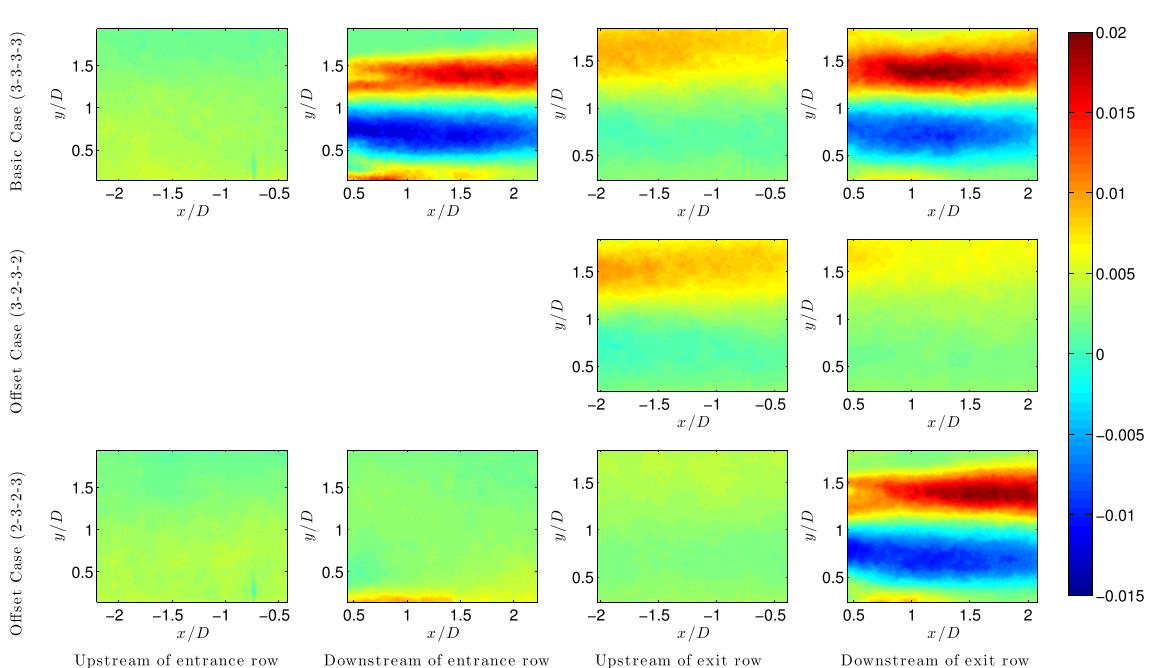


**Figure 4.** Contour plots of  $-\bar{uv}/U_{hub}^2$ , where  $U_{hub} = 4.6 \text{ m s}^{-1}$ .

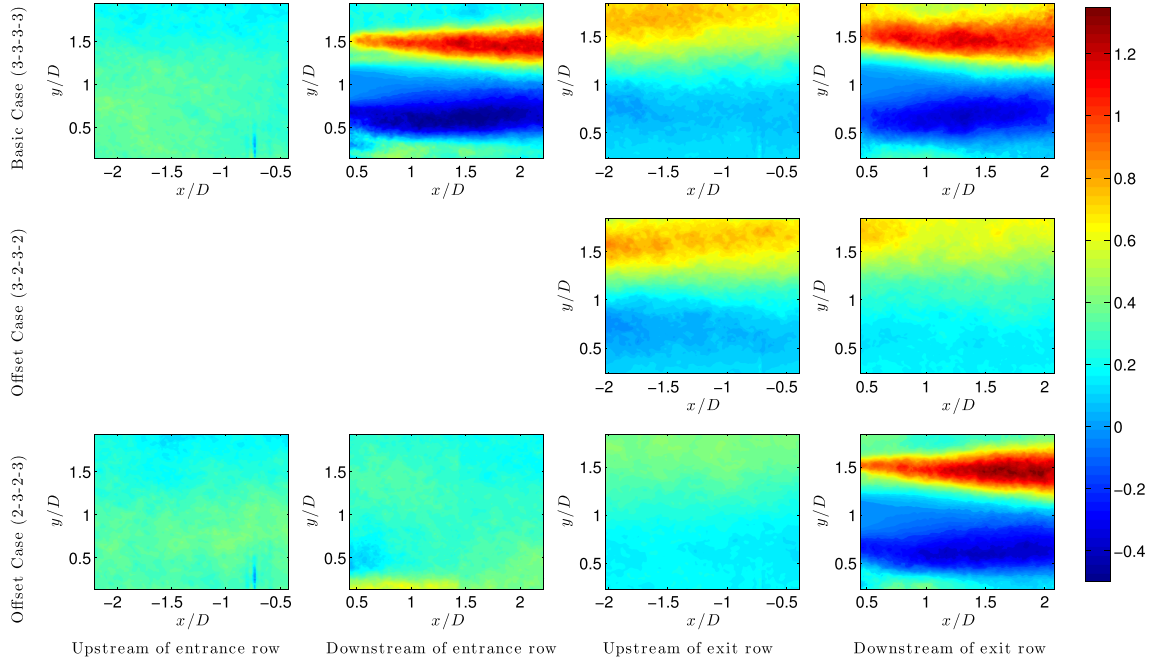


**Figure 5.** Contour plots of flux of kinetic energy,  $F_{ij}(\mathbf{x})$ . Here,  $F_{12} = -\bar{uv}U$  is shown as it is the dominant contributor to the whole.

The production and flux of turbulence kinetic energy arise as the second and third terms in right-hand side of equation (14). In the case of a wind turbine array operating under the given conditions, the pressure gradient is typically considered to be small compared to the production and flux terms and the mechanical power extracted by the wind turbines.

Energy is drawn from above the turbine canopy into the momentum deficit areas of the wakes through the flux of kinetic energy,  $F_{ij}(\mathbf{x})$ . Here, only the in-plane component of  $F_{ij}(\mathbf{x})$  is used,  $F_{12}(\mathbf{x}) = -\bar{uv}U$ . Previous research has demonstrated that this phenomenon is most active in the plane aligned with the rotor hub and parallel to the mean flow.<sup>15–18</sup> Figure 5 shows the flux of turbulence kinetic energy for all measurement locations. Note that in the wake of BCB,  $F_{12}(\mathbf{x})$  is active across a larger area than in the other wake areas. This delocalization is due to the momentum deficit present above the wind turbines deep into the array, leading to softened gradients of the streamwise velocity. Also interesting to note in the contours corresponding to OC1,  $F_{12}(\mathbf{x})$  is still active in entraining high-velocity fluid into the main wake area, demonstrating that wakes are not fully recovered 10–12 rotor diameters downstream.

Part I of the paper presents and discusses statistical values for the mean streamwise velocity,  $U$ , and the production of turbulence kinetic energy,  $P_{ij}(\mathbf{x})$ , in greater detail. Most of the results and detailed discussions are not repeated in this paper for brevity. However, the results pertaining to  $F_{12}(\mathbf{x})$  are included for reference as low-dimensional reconstructions are undertaken in the succeeding text.  $P_{ij}(\mathbf{x})$ , from the perspective of wind turbines, can be thought of as a measurement of mean kinetic energy that is being made unavailable to successive devices in the array. This is based on the insight that wind turbines extract mechanical energy from the mean flow rather than from turbulence directly. Low-dimensional descriptions of  $P_{12}(\mathbf{x})$  are undertaken in later sections of the current research.

#### 4.2. POD results

The eigenvalues,  $\lambda_n$ , obtained from the analysis are discussed first as they relate scales of turbulence on the basis of energy content. Recalling that the sum of the eigenvalues is equal to the mean turbulent kinetic energy in each measurement location (equation (12)), selecting a threshold of energy denoted by the eigenvalues is equivalent to selecting sets of turbulent structures containing the same level of turbulent energy.

For easy comparison of  $\lambda$  for each location, a percentage contribution of successive eigenvalues is shown in Figures 6 and 7. The successive percentage contribution is written,

$$E_n = \frac{\sum_{k=1}^n \lambda_n}{\sum_{l=1}^{2000} \lambda_l}, \quad n = 1, 2, \dots, 2000 \quad (15)$$

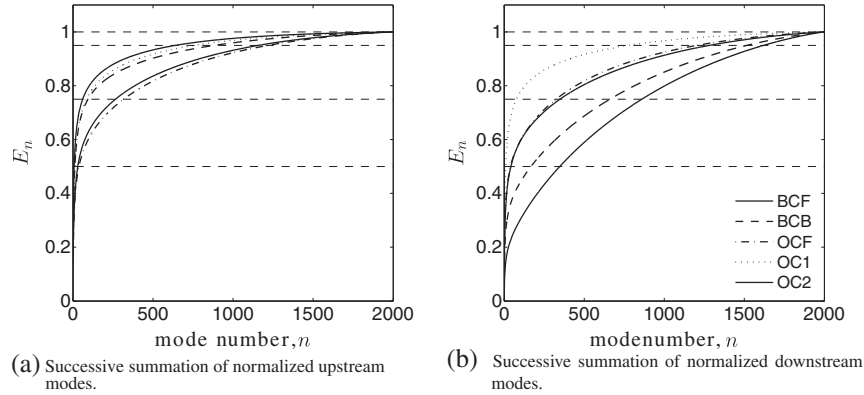


**Figure 6.** Successive summation of normalized modes,  $E_n$ . Locations where energy converges to the full turbulent kinetic energy faster demonstrate a sharper bend. A more even distribution of energy in eigenvalues show as slower convergence as in the downstream trends of BCF and BCB.

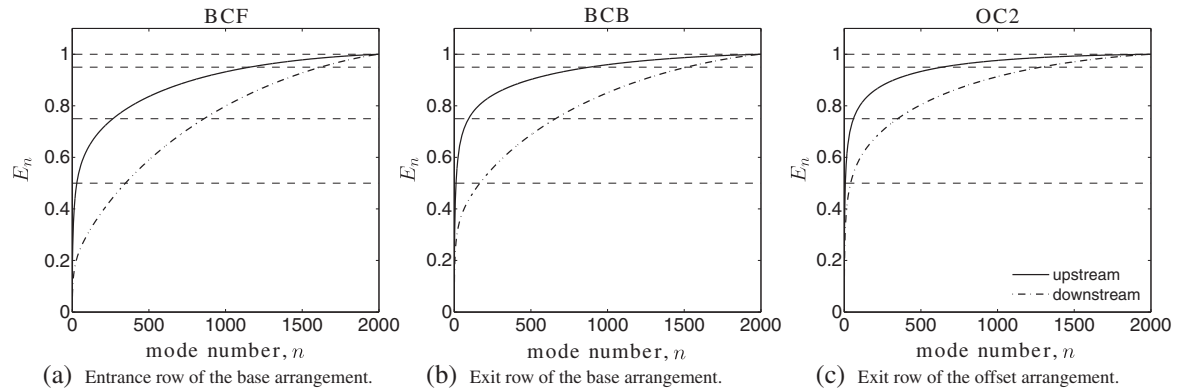


**Figure 7.** Side by side comparison of the successive sum of energy contained in modes,  $E_n$ , for wind turbine locations. Greater range of turbulent scales leads to delayed convergence of  $E_n$  to 1.

**Table I.** Modes required to reconstruct a prescribed portion of turbulence kinetic energy (upstream-downstream).

	BCF up-down	BCB up-down	OCF up-down	OC1 up-down	OC2 up-down
Modes for 50% energy	30–348	13–168	38–39	13–10	8–42
Modes for 75% energy	266–860	94–661	317–324	85–77	61–349
Modes for 90% energy	789–1370	488–1222	857–845	404–410	323–918
Modes for 95% energy	1158–1621	883–1561	1219–1204	758–776	640–1282

Recall a total of 2000 POD modes for each position are used.

and describes the cumulative energy contained in the first  $n$  modes normalized by the total energy in that location. Each case requires the full set of 2000 modes to rebuild the full turbulence kinetic energy according to equation (12). The figure also shows prescribed levels (50%, 75%, 95% and 100%) of energy as dashed horizontal lines. Points where the curves of  $E_n$  cross the horizontal thresholds correspond to the values in Table I. Note that cases that converge to given thresholds with fewer modes are those in which the relative energy contained in large scales is greater. Slow convergence to the full turbulence kinetic energy suggests that the dominance of the energetic modes is less pronounced.

Figure 7 shows the successive summation of eigenvalues for the three turbine positions in the arrays. Each subplot compares  $E_n$  for the upstream (solid line) and downstream (dashed line) of the turbines. In every case, the upstream set of eigenvalues converges more quickly than the downstream position. For the measurement locations without turbines

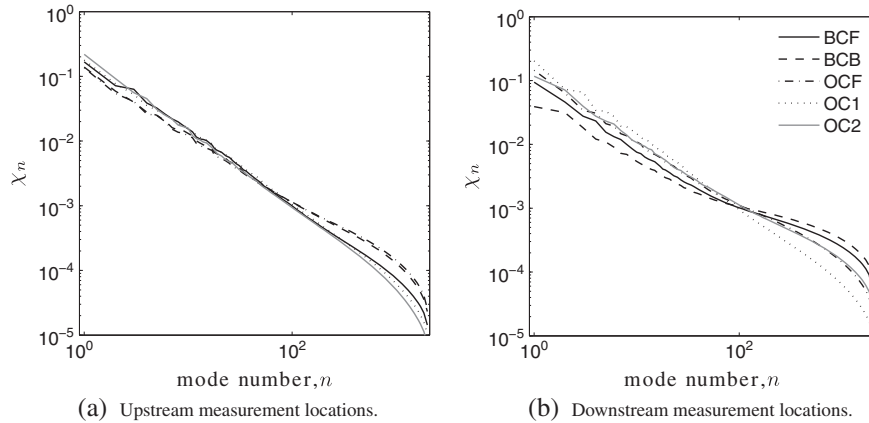


**Figure 8.** Comparison of normalized eigenvalues  $\chi_n$  values for each measurement position. Note that the first mode for all cases is higher downstream than upstream. Trends shown in log scale and demonstrate a slope of  $-1.2$  for large and intermediate scales.

(OCF and OC1, not shown), the upstream and downstream trends are virtually identical as the turbulence kinetic energy is very similar in both positions. Without a turbine rotor to influence the relative content of energy in each scale, the turbulence is not expected to evolve significantly in a short downstream distance (approximately three rotor diameters). The slight differences seen in the two positions of OC1 are due to the development of turbulent structures as the flow moves downstream.

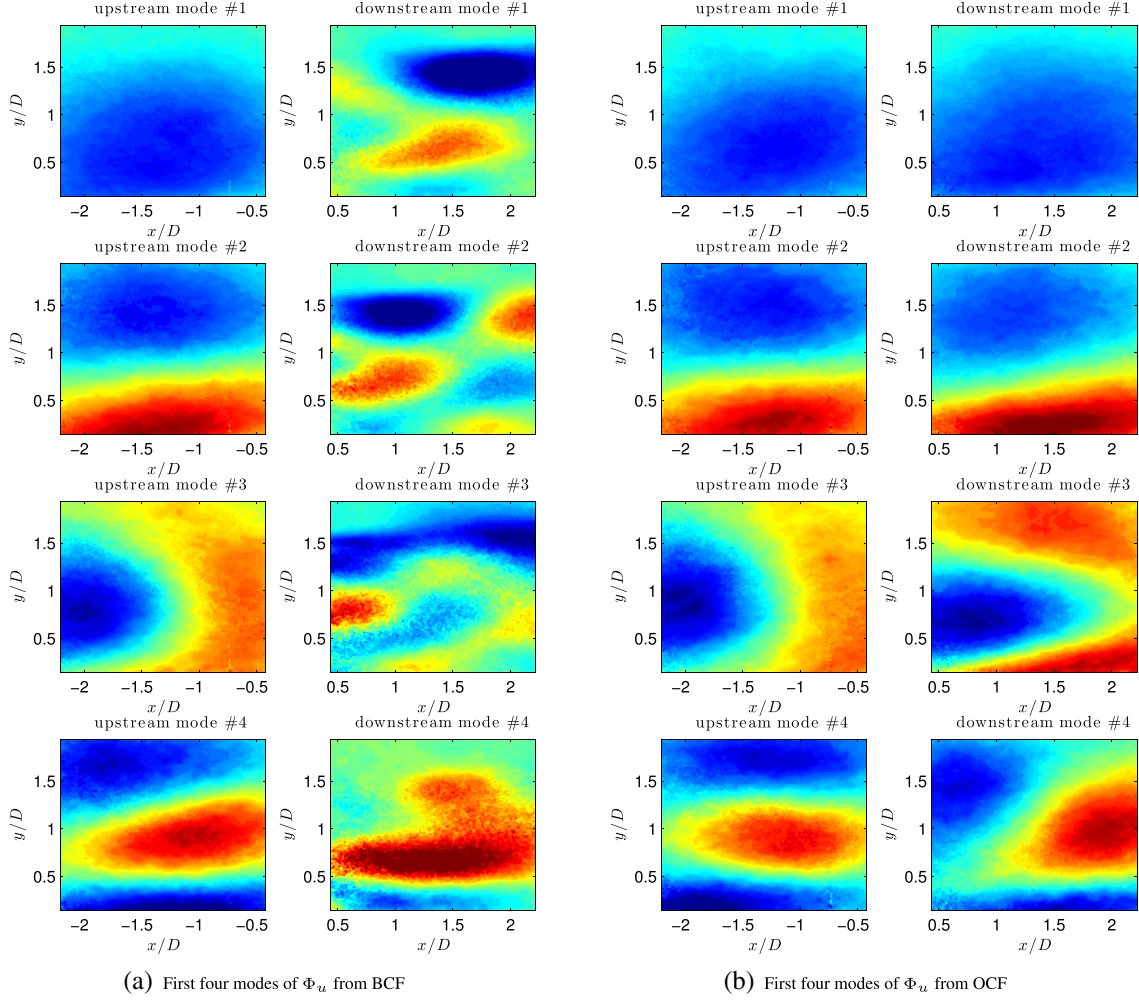
An alternate presentation of the distribution of energy contained in the eigenvalues of the POD is presented in Figure 8. In the figure, the eigenvalues are self-normalized, such that for each case,  $\chi_n = \lambda_n / \sum_{i=1}^N \lambda_i$  and  $\sum_{i=n}^N \chi_n = 1$ . In the downstream measurement location as shown in Figure 8b, positions following wind turbines show a strong deviation from the  $n^{-1.2}$  trend seen in the low mode numbers. The increase of energy contained in high mode numbers is attributed to the energy directed into smaller scales through the rotation of the turbine rotor.

Table I details that the upstream position of each measurement location reaches the 50% threshold with fewer modes than the downstream position with the exception of the exit row position in the (3-2-3-2) offset arrangement. This agrees well with expected results as the turbulence is more organized before the turbine. Upstream of the turbine, scales larger than turbine blade carrying a relatively large amount of energy are prevalent. As the flow moves through the turbine, the blades reduce the size of the large, organized scales, and the POD requires more modes to reach a given threshold of energy. In the case of OC1, the upstream window requires more modes to reach the 50% and 75% thresholds of turbulence energy than the downstream measurement window. This position corresponds to the far-wake of the third turbine row in the offset array. By this point in the wake, the effect of the turbine disappears, and turbulence re-organizes itself in such a way that the large scales become more dominant. Additionally, the level of turbulence in this location is increasing due to the growth of a boundary layer internal to the turbine canopy layer.

To rebuild 50% of the energy in the inflow, between 0.4% (OC2) and 1.9% (OCF) of the modes are required. For the outflow, up to 17.4% of the modes are required to reach the 50% threshold, as in BCF. The inflow of OC2, an exit row position *with* a turbine, has had 12 rotor diameters to recover. This is also the position requiring the fewest modes to reconstruct 50% of turbulent energy, approximately 20–30% of the modes required to reach the same energy level for inflow to the turbine array.

When the input data for the POD is homogenous, the resulting POD modes reduce to Fourier modes. In positions where there is at least a *weak* homogeneity, the POD modes demonstrate some Fourier-like behavior. This is evident in the low modes in downstream windows of the entrance row turbine locations as seen in Figure 9. In such positions, the gradients in the streamwise direction are very small compared with the wall-normal direction. The POD modes of the entrance row of the base case (BCF) shown in Figure 9 demonstrate a mixture of POD and Fourier modes in the streamwise direction. As yet, these modes do not represent velocity fluctuations. It is only when they are multiplied by their respective coefficients,  $a_n$ , according to equation (9) that the magnitudes of the modes become representative of flow statistics.

Also illustrated by the figure is the effect of the rotor blade on the POD modes of the flow. In Figure 9(b), the upstream and downstream modes of  $\Phi_u$  are nearly identical as the only physical change in the flow geometry is from the mounting plate for the turbine models on the floor of the wind tunnel. This difference is seen most clearly as a distortion of the third and fourth downstream modes. Comparing these with the downstream modes corresponding to a turbine position in Figure 9(a), the organization is lost from upstream to downstream measurement locations. As the turbine rotates on its axis, periodic forcing from the blades is shown in the measurement domain. At this point, the turbulent boundary layer is mixed



**Figure 9.** Comparison of upstream and downstream scalar POD modes corresponding to the streamwise direction for both entrance row measurement positions. Upstream modes in the left column of each subfigure are nearly identical between cases. Downstream modes vary greatly because of the presence of a wind turbine in BCF (a). Upstream and downstream modes for empty array positions are very similar as flow has changed little between measurement locations reference to subfigure (b). Although the color scale information is identical for every shown mode ( $-0.015 \leq \Phi_u \leq 0.015$ ), the color bar has been omitted because the modes are not physical until multiplied with their respective coefficients.

with a wake-like flow, which is periodic in the azimuthal sense. Therefore, modes have shapes like one would observe in homogeneous directions.

The POD executed in this research uses a kernel built with the streamwise and wall-normal components of the velocity. The streamwise POD modes,  $\Phi_u$ , shown in Figure 9, may be combined with the wall normal POD modes,  $\Phi_v$ , in a vectorial sense as in Figure 10. The modes  $\Phi_u$  and  $\Phi_v$  are orthogonal in a *physical* sense, whereas sequential modes (indexed with  $n$ ) are orthogonal in the sense of linear algebra.

The POD modes of BCF shown in Figure 10 are vectorial combinations of the scalar POD modes and unit vectors in the streamwise and wall-normal directions ( $\mathbf{e}_x$  and  $\mathbf{e}_y$ , respectively) as,

$$\Phi = \Phi_u \mathbf{e}_x + \Phi_v \mathbf{e}_y \quad (16)$$

and give a better sense of the flow structures highlighted in the current analysis. As seen in the figure, the low mode numbers (Figure 10(a),(b)) demonstrate structures on the scale of the measurement window upstream and of the scale of the rotor downstream. Although the POD does not directly lend length and velocity scales, the modes do provide some indication of persistent and energetic forms within the flow. Progressing in mode number (Figure 10(c)–(f)) quickly leads to more

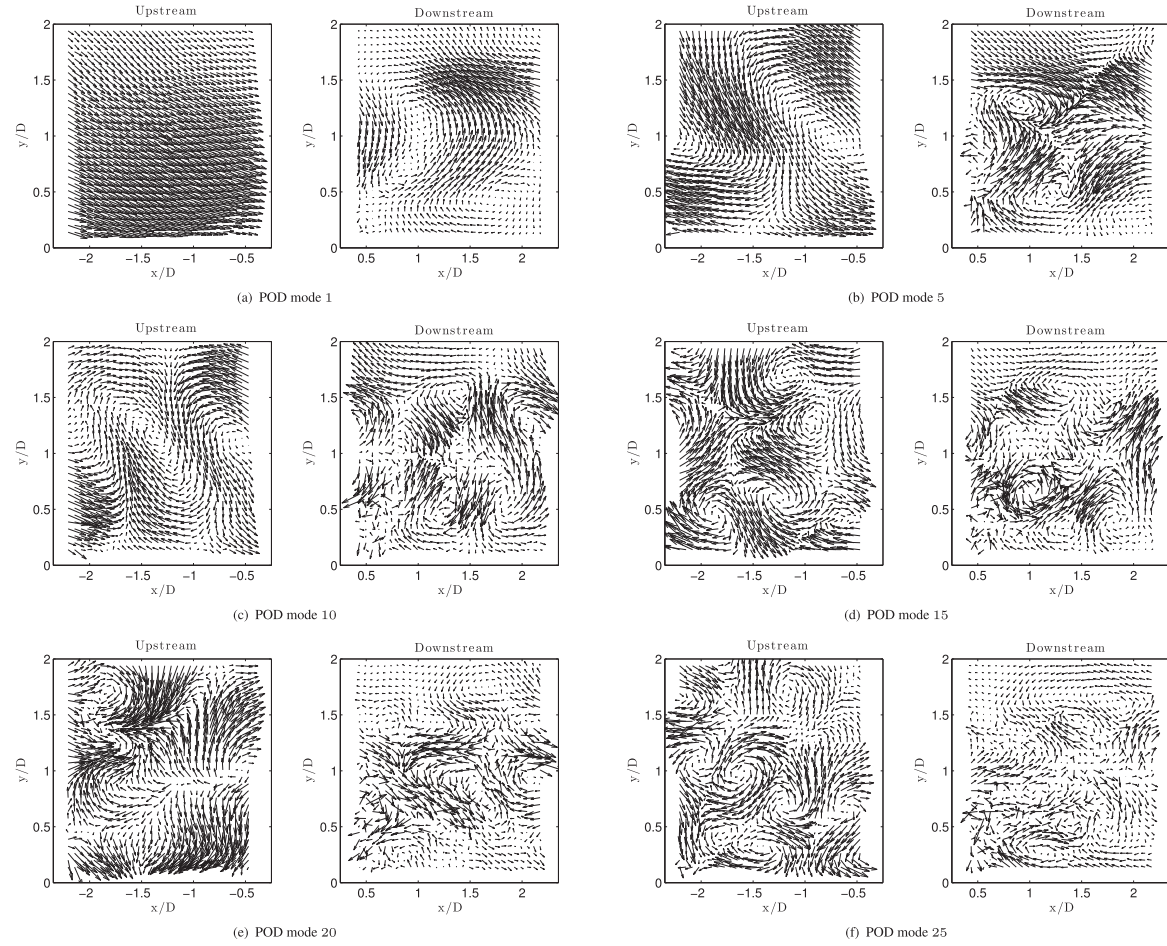


**Figure 10.** Vectorial POD modes composed of both  $\Phi_U$  and  $\Phi_V$  from BCF. Each pair of subfigures correspond to individual modes as noted in captions. Upstream POD modes demonstrate larger, more organized structures throughout the decomposition. Downstream POD modes exhibit a greater range of structure size and complexity. Activity in the downstream window is most significant in the rotor area of the wake.

complex structures whose apparent scales drop off quickly to the chord length of the rotor and smaller. The separation between large, energetic structures leads to the low-dimensional descriptions discussed below.

The POD modes shown in Figures 9 and 10 are demonstrative of the orthogonal vector basis produced by the POD. The magnitudes of the modes have no physical relevance on their own. According to equation (10), the coefficients,  $a_n$ , are obtained by projecting the original stochastic velocity data onto the basis of deterministic POD modes and integrating over the measurement domain. Fluctuating velocity fields can then be reconstructed according to equation (9). By inference, one can use a subset of the POD modes to reconstruct velocity fluctuations with a portion of the total turbulent kinetic energy determined ahead of time.

Figure 11 shows Reynolds stress reconstructions with selected numbers of modes. From left to right are the Reynolds stresses  $\bar{u^2}$ ,  $-\bar{uv}$ , and  $\bar{v^2}$ . The contours of mean stresses presented in the figure correspond to the exit row of the base arrangement, BCB. Moving from top to bottom, the stresses shown are composed of 5, 10, 25, 50, 100 and 200 modes, respectively. Note that when comparing the Reynolds stresses in the figure with those presented in *Part I* of the paper and in Section 4.1, one can see that relatively few modes are required to achieve intensities on the same order as the original data.

After only five modes, all three stresses ( $\bar{u^2}$ ,  $-\bar{uv}$ , and  $\bar{v^2}$ ) already show the structure seen in statistical quantities like the mean stresses. The same color scale was used in Figure 11 as in Figure 4 for ease of comparison. The energy contained in stresses  $\bar{u^2}$  and  $-\bar{uv}$  reconstructs very quickly, whereas  $\bar{v^2}$  requires many more modes to match the original statistical values. This is indicative that the turbulent energy in the wall-normal fluctuations is distributed across a larger number of modes than the streamwise fluctuations and more energy is excluded from the reconstructions.

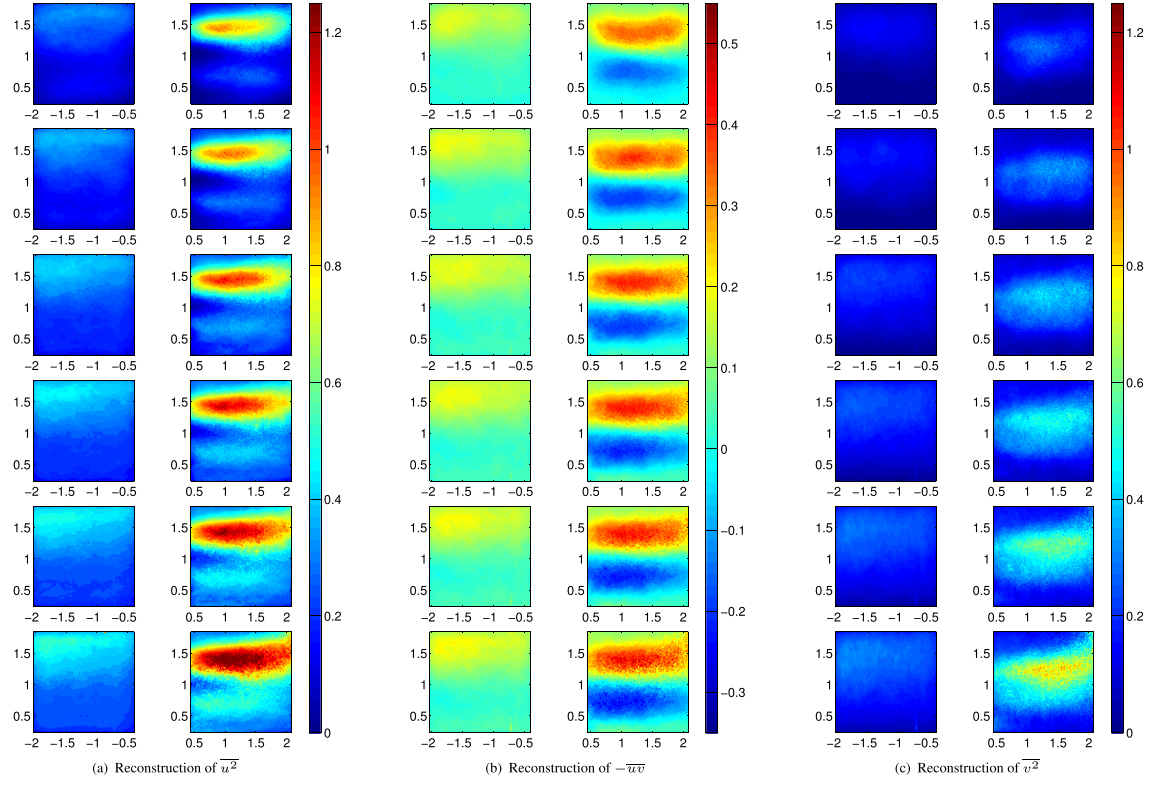


**Figure 11.** Reconstruction of mean Reynolds stresses. Velocity reconstructions are composed of POD modes  $\Phi_U$  and  $\Phi_V$  according to equation (9). The number of modes used in the reconstructions by row from top are 5, 10, 25, 50, 100 and 200.

#### 4.3. Reconstruction and low-dimensional description

Reduced-order reconstructions in the following analysis are those comprised of a limited set of POD modes based on the ordered set of eigenvalues. Several approaches are taken in the creation of such models. The first approach to reconstruction is considering a specific portion of the total turbulence kinetic energy according to the eigenvalues,  $\lambda_n$ . Most commonly, statistical quantities are reconstructed using only the POD modes required to assemble 50% of the full turbulence kinetic energy. Reconstructions in this sense can be to any prescribed percentage of the total energy in the measurements. Table I shows the number of modes required to reach several levels of the energy at each measurement location.

Figures 12 and 13 show  $F_{12}(\mathbf{x})$  calculated with the reconstructions of  $-\bar{uv}$  limited to 50% of the energy in the flow as detailed by the eigenvalues,  $\lambda_n$  (shown in Table I). In the figures, the reconstructed flux of kinetic energy is nearly identical to the calculations shown resulting from statistics of measurements. This is demonstrative that the vertical entrainment of kinetic energy is reliant predominantly on the large structures of turbulence. The increased energy of large scales associated with the top-tip of the rotor tends to increase the energy entrained from above the canopy into the momentum deficit area of the wake.

Figure 13 shows the 50% reconstruction of  $F_{12}(\mathbf{x})$  only in the near wakes of the three wind turbine positions measured in the experiment, BCF, BCB and OC2. Although each mode has a net positive contribution to the total turbulence kinetic energy in the field as denoted by  $\lambda_n$  and shown in Figures 6 and 8, modes may make negative local contributions to stresses. The reconstructions shown in Figure 13 show an overestimation of the flux of kinetic energy compared with the original statistical data. The implication of this is that the intermediate and small scales (associated with large mode numbers) make a contribution to  $F_{12}(\mathbf{x})$  that is opposite the trend seen in the mean statistics.

The overestimation of energy contained in statistics is avoided by imposing a convergence criterion on the reconstructions as previously discussed. On the basis of the observation that power extracted by a wind turbine can be related directly to the flux of kinetic energy across the rotor area in the wake,<sup>15</sup> reconstructions were made to approach the span of the Reynolds stress  $-\bar{uv}$  averaged along the streamwise coordinate. That is, the number of modes,  $n$ , was determined to satisfy the 95% criterion outlined in the following text.

The second approach to low-dimensional representations is based on the maximum span of the streamwise averaged profile of the Reynolds shear stress,  $-\bar{uv}$ . As the downstream measurement windows correspond only to the near wake,

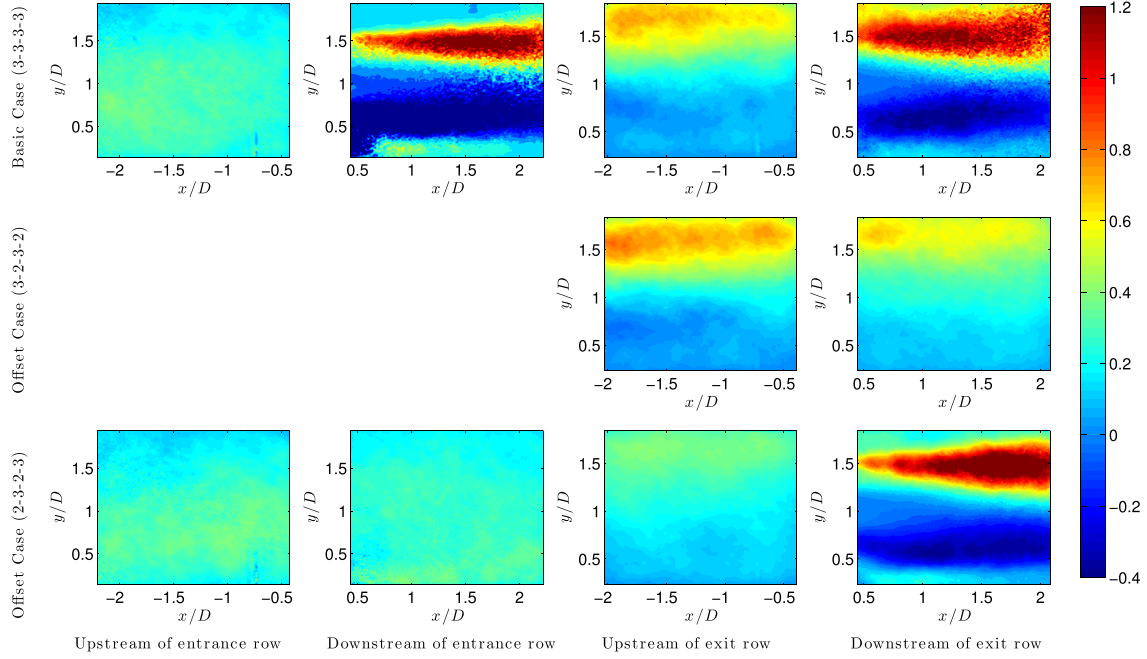


**Figure 12.** Reconstructions of the flux of kinetic energy,  $F_{12}(x)$ , for all measurement positions. Plotted data is comprised of  $-\bar{uv}$  with only the modes containing the first 50% energy, and the mean velocity field  $U$  from SPIV results in *Part I* of the paper.

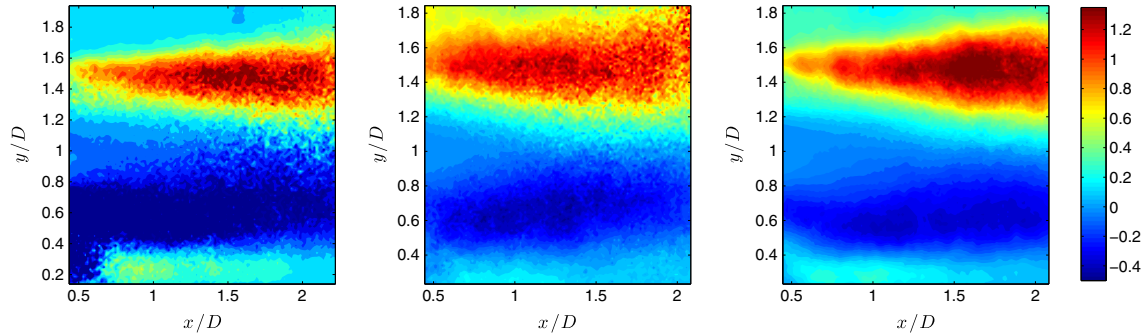


**Figure 13.** Reconstructions of the flux of kinetic energy  $F_{12}(x)$  for the immediate wake areas. Plotted data is the same as in Figure 12. From left to right are the cases BCF, BCB and OC2, the entrance and exit rows of the base arrangement, and the exit row of the second offset arrangement, respectively.

the streamwise average of  $-\bar{uv}$  can be considered an effective and representative profile at each location taken into the consideration while averaging. Streamwise averaging over a PIV window will hereby be denoted with angle brackets and an  $x$  subscript as,  $-\langle \bar{uv} \rangle_x$ . The successive addition of POD modes to reconstructed statistics leads to a net positive addition to the range of dynamics for each quantity. Thus, a convergence criterion can be set by considering the span of  $-\langle \bar{uv}_n \rangle_x$ , where the subscript  $n$  refers to the number of POD modes used in the reconstruction.

A goal of performing the snapshot POD analysis on the data here was to determine which structures are most significant in the performance of the wind turbine models and the dynamics within the wind turbine canopy layer. The flux of kinetic energy,  $F_{12}(x)$ , and the turbulence production,  $P_{12}(x)$ , discussed in Section 4.1 are especially important in the recovery and dynamics of the boundary layer pertaining to wind turbine arrays.

Profiles of the streamwise-averaged Reynolds shear stress,  $-\langle \bar{uv} \rangle_x$ , compared with its reconstructions with successive summations of modes are shown in Figure 14. The black line in each of the following figures is the streamwise average of statistical data from Section 4.1, and gray lines are reconstructions. Only the wake areas (BCF, BCB and OC2) are shown as they are the areas of interest in the following low-dimensional representations.

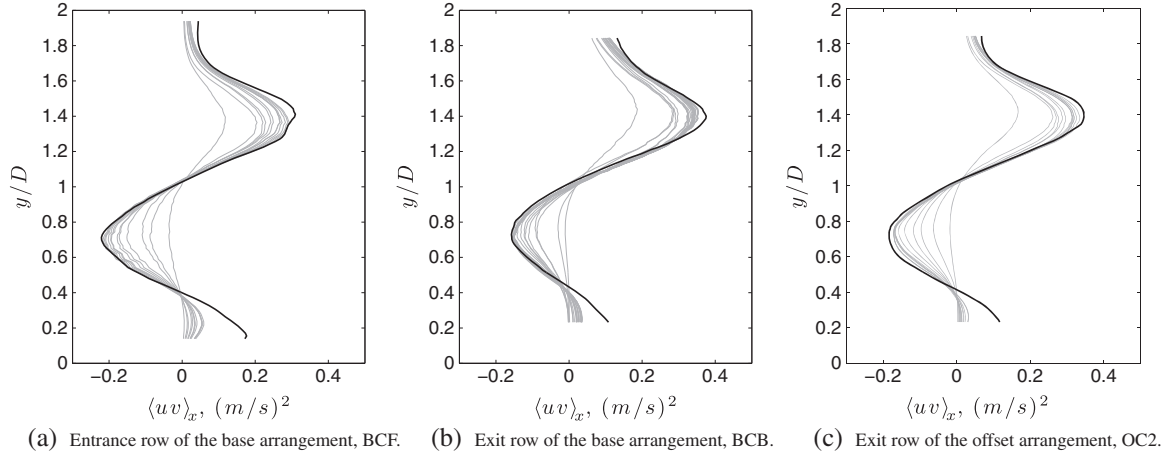


**Figure 14.** Streamwise average profile of  $-\langle uv \rangle$ . Black line is  $-\langle uv \rangle_x$  from SPIV statistics. Gray lines are reconstructions,  $-\langle uv_n \rangle_x$  with successive inclusion of modes.

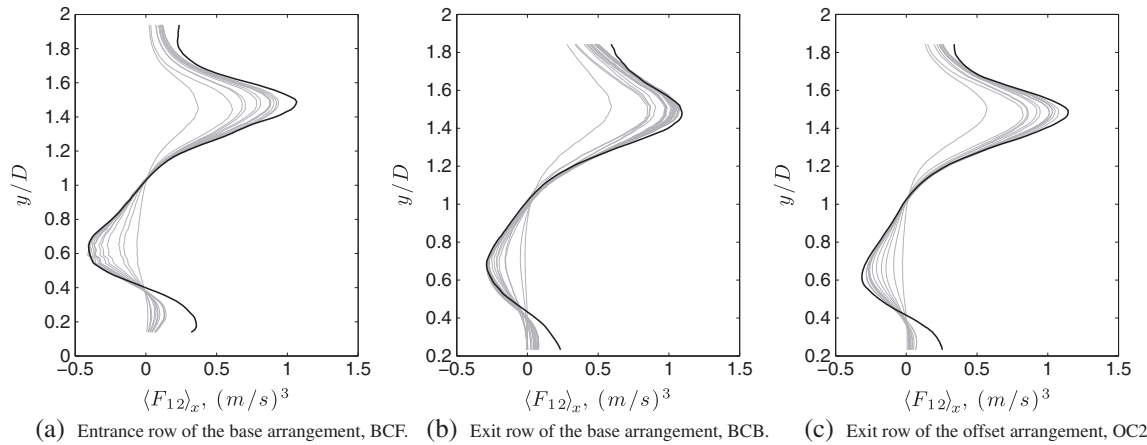


**Figure 15.** Streamwise average profile of  $F_{12,x} = -\langle uvU \rangle_x$ . Black line is  $-\langle uvU \rangle_x$  from SPIV statistics. Gray lines are reconstructions,  $-\langle uv_n U \rangle_x$  with successive inclusion of modes.

Meeting the aforementioned criterion for reconstruction correlates well with the condition of the inflow to each particular wind turbine. Where the inflow is the undisturbed inflow boundary layer (BCF) or a well-recovered wake (OC2), the reconstruction according to this scheme takes 12 and 13 modes, respectively. In contrast, in the turbine position with a large momentum deficit and greater turbulence as inflow, as in the exit row of the base configuration BCB, the same reconstruction takes 25 modes. In every case, the turbulent structures associated with the top-tip rebuild much more quickly than those associated with the bottom tip of the rotor, most notably in the exit row turbines. The difference in reconstruction rates from top-tip to bottom-tip areas of the wake is due to the presence of the turbine mast in the bottom area. The mast causes additional turbulence and mixing in that area.

The profile composed of only the first mode is nearly vertical for BCB and OC2 below the hub ( $y/D \leq 1$ ). As reflected in the POD modes in Figures 9 and 10, the contribution of low modes to the profile is more significant than that of higher mode numbers. The tip vortices shown in the original statistics (Figure 4) is missed in the reconstruction of BCF as it relies on smaller scales associated with higher mode numbers.

Applying a similar approach of streamwise averaging and reconstruction with successive modes to the flux of kinetic energy,  $F_{12}(x)$ , yields the profiles in Figure 15. Here, the Reynolds shear stress was composed of a limited number of POD modes, and the mean streamwise velocity,  $U$ , was taken from the original statistics. Similar trends are found for the flux of kinetic energy as observed for the reconstructions of the Reynolds shear stress. However, in these profiles, the exit row of the base configuration rebuilds accurately with few modes due to the streamwise homogeneity of  $-\overline{uv}$  at that location.

The near-wall region where  $F_{12}(x) > 0$  does not reconstruct well given the current approach. This meets the theory as the turbulence there is composed of smaller scales that are associated with intermediate and high-mode numbers.

The final quantity approached with the current low-dimensional reconstruction scheme is the turbulence production,  $P_{12}(\mathbf{x})$ , seen in Figure 16. The production of turbulence in Figure 16 shows that the only regions of significant production are those associated with the tips of the rotor blades (see contours and profiles in *Part I* of the paper, for reference). The two peaks shown in the profiles of streamwise-averaged production reflect this well. It can also be seen from the reconstructed profiles that production near the top-tip is associated more closely with large structures as it rebuilds very quickly with very few modes. In contrast, profiles of  $P_{12}(\mathbf{x})$  near the bottom tip show very little activity with the first few modes.

#### 4.4. Power study and the POD

The curves of the power coefficient shown in Figure 17 demonstrate that the exit row turbine in the offset case has a greatly increased peak  $c_p$  value over that of the base case. Conservation of energy principle indicates that the mechanical energy extracted from a flow should be on the same order of magnitude as the difference in mean flow kinetic energy between

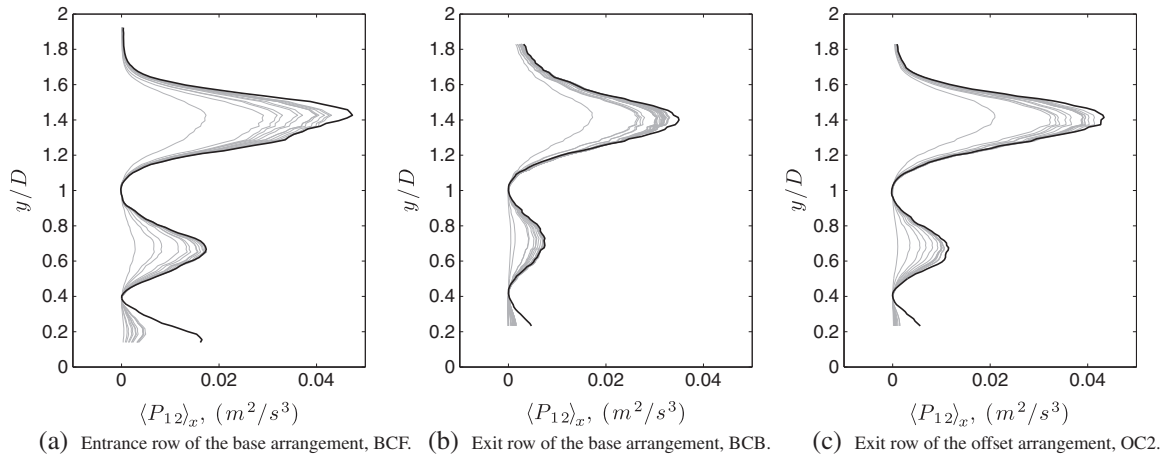


**Figure 16.** Streamwise average profile of  $-\langle uv \rangle \frac{\partial U}{\partial y}$ . Black line is  $-\left\langle \overline{uv} \frac{\partial U}{\partial y} \right\rangle_x$  from SPIV statistics. Gray lines are reconstructions,  $-\left\langle \overline{uv}_n \frac{\partial U}{\partial y} \right\rangle_x$  with successive inclusion of modes.

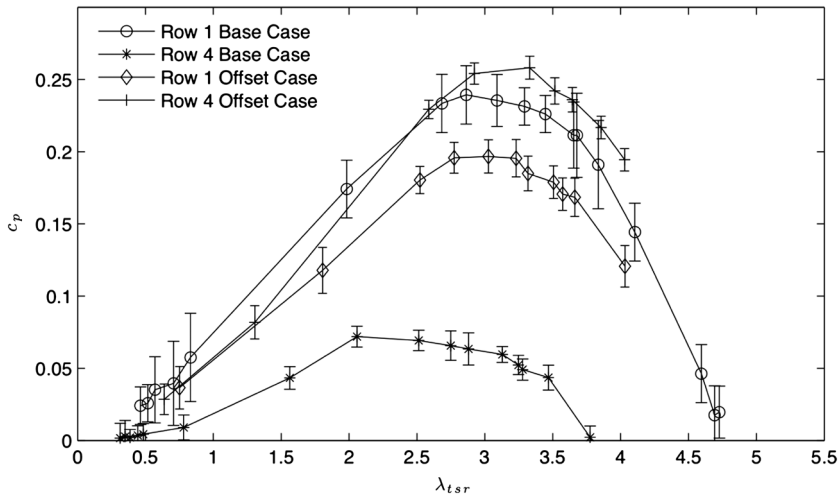


**Figure 17.** Curves of the power coefficient,  $c_p$ , for the entrance and exit row wind turbine models. Values of  $c_p$  for both offset cases are included. The entrance row of the offset data (+) corresponds to the (3 – 2 – 3 – 2) configuration, and the exit row (\*) represents the (2 – 3 – 2 – 3) configuration. Error bars represent the variance of the signal for each measurement.

upstream and downstream locations. It is also well understood that large-scale turbulence can have a significant effect on the productivity of a wind turbine. It is through this understanding that the POD is compared with the power coefficients of the wind turbines.

It has already been observed that the lower POD modes demonstrate a concentration of relative energy content compared with the full span of modes when moving downstream within the array. The reduced-order reconstructions previously discussed relate the ability of the POD to capture quantities representative of power entrainment and loss as seen in Figures 15 and 16. The implication of these data is that the performance of turbines in different arrangements may be assessed or estimated by the eigenfunctions and eigenvalues resulting from the POD.

Figure 18 shows the ratio of energy contained in successive modes upstream and downstream of the wind turbines,

$$\kappa = \frac{\lambda_{n,\text{upstream}}}{\lambda_{n,\text{downstream}}}. \quad (17)$$

This relationship demonstrates that the energy contained in upstream modes falls off faster than downstream modes. For instance, the trend line showing  $\kappa$  for the exit row of the offset case (OC2) shows that the ratio of upstream to downstream POD eigenvalues is lower than the base case for low POD numbers. Thus, there is a larger difference in the energy carried by POD modes in the upstream and downstream measurement windows as compared with the base arrangement. In the exit row of the base arrangement, BCB,  $\kappa$  is greater than that of the entrance row. For low mode numbers ( $n < 12$ ),  $\kappa$  is closer to a unity value than for the other two cases. This implies that the energy contained in POD modes upstream and downstream are nearly equal.

At downstream locations, the level of turbulence is increased by the action of the turbine blades. Therefore, it is seen that  $\kappa$  is smaller than 1 for intermediate and high-mode numbers ( $n \geq 12$ ). If the importance of different scales were to stay the same, then we would see a constant ratio for every POD mode number. However, it seems that there is almost a constant ratio between the upstream and downstream eigenvalues up to mode number 12; the weight of the smaller scales downstream of the wind turbines increases after mode 12. Therefore,  $\kappa$  decays in Figure 18. As seen in the Figure, the decay rates of BCF and BCB are very close to each other. A slower decay is seen in OC2, suggesting that the higher POD modes get less energy relatively.

Assessing the total turbulence kinetic energy through the POD is a matter of summing the eigenvalues according to equation (12). In doing so, a global estimate can be made of the turbulence in upstream and downstream positions

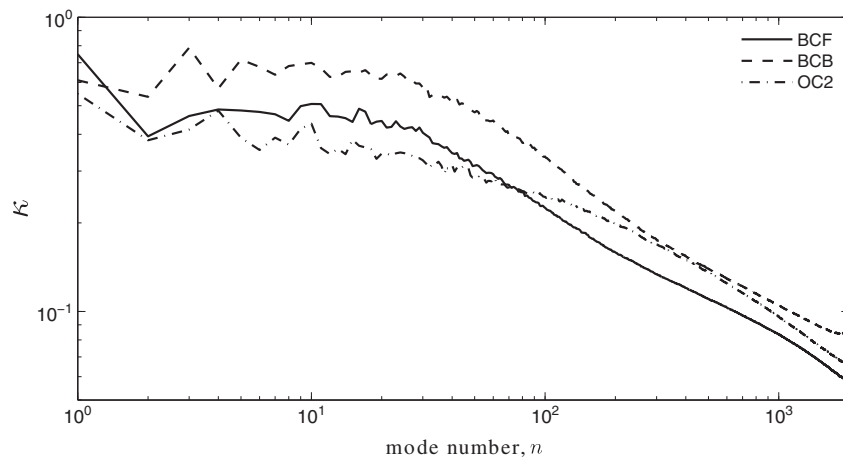


**Figure 18.** Comparison by mode of the ratio  $\kappa$  for each wind turbine in the arrays highlighting the difference in relative importance of turbulence scales outlined through the POD. A higher ratio of  $\kappa$  at high-mode number indicates that more energy is converted from the mean flow and large-scale turbulence to small scales.

**Table II.** Ratio of sums of eigenvalues in upstream and downstream measurement locations.

Measurement case	$\kappa$
BCF	0.2100
BCB	0.3439
OC2	0.2933

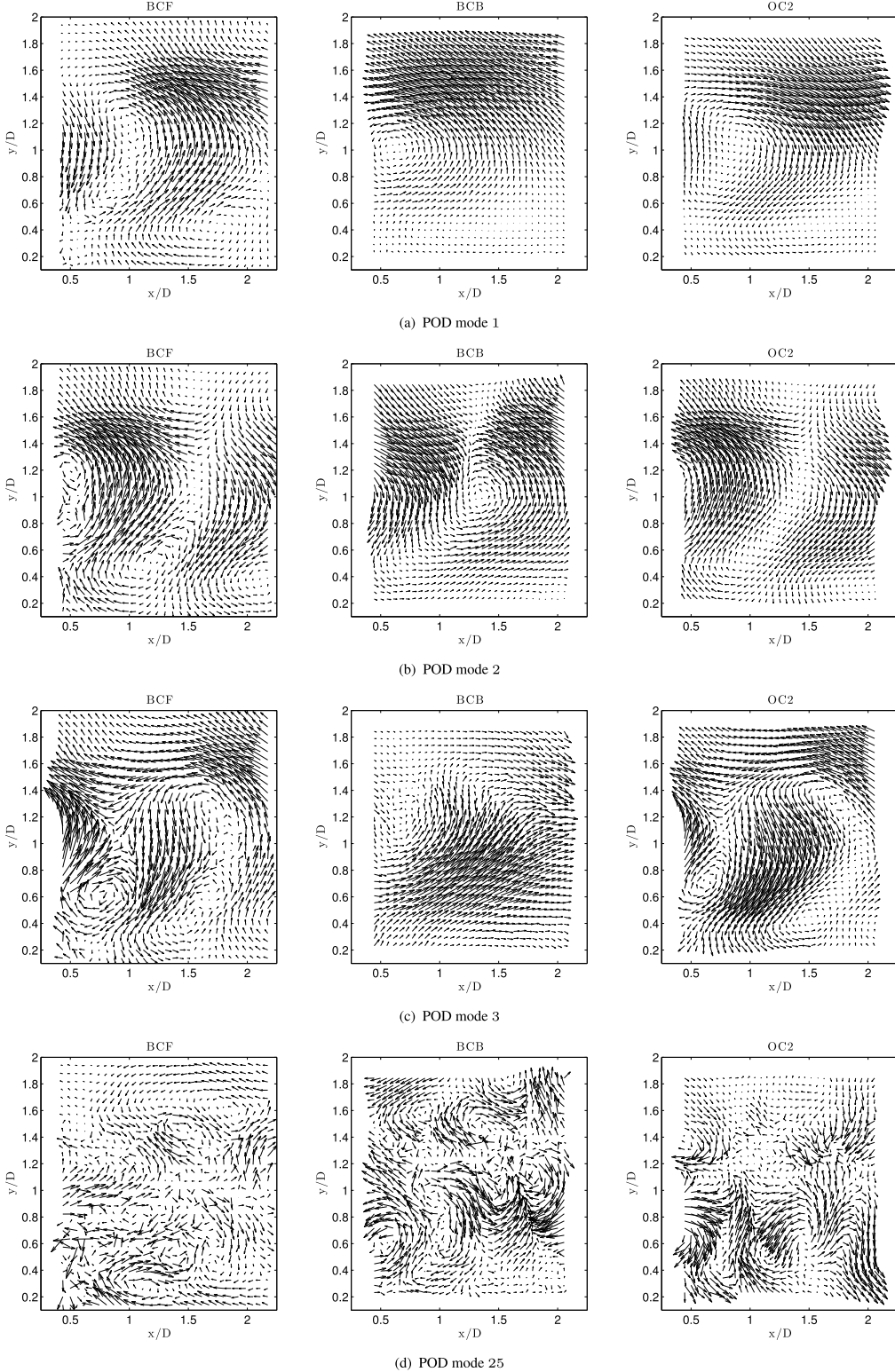


**Figure 19.** Vectorial POD modes in measurement locations immediately downstream of turbines. The leftmost column of subfigures corresponds to the front row turbine, BCF. Center and right columns correspond to the exit row turbines of the Cartesian (BCB) and row-offset (OC2) cases, respectively. Strong similarity of the exit row of the row-offset case to the entrance row turbine can be seen in the first three modes.

relative to the turbines. Table II shows the ratio of eigenvalue summations upstream and downstream of the turbines according to equation (18).

$$\mathcal{E} = \frac{E_{upstream}}{E_{downstream}} = \frac{\sum_{n=1}^{2000} \lambda_{upstream}}{\sum_{n=1}^{2000} \lambda_{downstream}} \quad (18)$$

Comparing the peak  $c_p$  values from Figure 17 to the values in Table II shows that smaller magnitudes of  $\mathcal{E}$  correspond to greater maximum power coefficient. This agrees with expected results in that  $\mathcal{E}$  relates the turbulence energy upstream and downstream of the wind turbines. Theory suggests that wind turbines extract energy from the mean flow field, especially the streamwise direction  $U$ . The comparison of turbulence energies upstream and downstream of turbines can be used to gage the efficiency of a wind turbine within an array.

To visualize the differences in behavior, Figure 19 compares directly the vectorial POD modes in outflow positions relating to the turbines previously discussed. In the first three POD modes (Figures 19(a)–(c)), one can see that the structures in BCF and OC2 are nearly identical. The vector fields relating to the exit row of the base case (center column) are similar to the other two but show less conformity to the other wakes. Figure 19(d) corresponds to the limiting mode for BCB according to the low-dimensional model previously suggested. It is included in the figure to show that the differences from case to case increase quickly with mode number. In the vector fields of BCF and OC2 at mode 25, there is less definition in the structures of the turbulent fields. This agrees well with the low-dimensional descriptions in the previous sections as the 95% criteria is met at mode 12 and 13, respectively.

## 5. CONCLUSIONS

The experiment presented and discussed compares the turbulence of entrance and exit row wind turbines with Cartesian and row-offset array configurations. The flow measurements show the difference of wakes and stresses produced in the interaction of wind turbines with the atmospheric boundary layer. Statistics of turbulence more closely reviewed and dynamical implications are discussed in *Part I* of the paper presented here.

The snapshot POD was applied to the SPIV measurements. From the resulting eigenvalues, it was observed that the distribution of turbulence kinetic energy across different POD modes varies considerably with measurement location and flow dynamics. The distribution of eigenvalues for each turbine demonstrate a similar behavior for upstream measurements where energy decays at approximately  $n^{-1.2}$ , and  $n$  is the POD mode number. The presence of wind turbines changes the distribution of energy among the modes greatly. In the wakes of turbines, intermediate and high modes contain a greater relative percentage of the total turbulence kinetic energy than measurement locations without turbines. Comparing the ratio of upstream and downstream eigenvalues with the curves of power coefficients for the wind turbine models suggests a connection between the energetic scales of turbulence and the power produced by wind turbine models.

Low-dimensional reconstructions of the flux of turbulence kinetic energy and turbulence kinetic energy production were approached through a convergence of the streamwise averaged profile of the reconstructed Reynolds shear stress,  $-\langle \bar{u}\bar{v}_n \rangle$ , to the profile obtained in the original data. It was shown that for turbines whose inflow is the undisturbed approach flow (BCF) or a recovered wake (OC2), approximately 0.6% of the total modes is required to reconstruct 95% of the span of  $-\langle \bar{u}\bar{v} \rangle$  in the wake. For wind turbines with a greater momentum deficit in the inflow (BCB), the reconstruction requires approximately twice the number of modes to reach the same convergence criterion.

These descriptions of turbulence statistics in the wakes of wind turbines and locations within the turbine array demonstrate also that much of the turbulent activity is in the region of the canopy near the top-tip of the rotors. Large scales in these locations contribute nearly all flux and production of turbulence kinetic energy. These results have immediate implications in the design and placement of turbines within new farms. As large scales of turbulence are responsible for both fatigue loading of blades and wake remediation, optimization of wind turbine efficiency requires that turbines be spaced to take advantage of a remediated flow. The staggered alignment of wind turbines as in the research presented here allows for an effective doubling of spacing between turbines in the streamwise sense and a reorganization of the turbulence beneficial for both power production and efficiency increases of the devices.

Additionally, the POD undertaken here can be applied to the development and verification of wind farm design software. As most numerical simulations of turbines and arrays use the actuator disc model, much of the modal information regarding the wakes is missed. The results presented here could be used to augment numerical simulations beyond the drag-element array modeling currently in practice.

The dependence of  $F_{ij}(\mathbf{x})$  and  $P_{ij}(\mathbf{x})$  on the spanwise velocity and spatial coordinate is not pursued here, as the objective of the current analysis was to find a reliable convergence criterion for low-dimensional models and snapshot POD. In order to diagnose the dependence of these turbulent mechanisms, measurements will be taken in spanwise planes across wind turbine wakes. Such measurements will also lead to direct assessment of asymmetry of entrainment of high-momentum flow from above the turbine canopy and the dissipation of mean flow energy into turbulence.

## ACKNOWLEDGEMENTS

The authors are grateful to the National Science Foundation's BRIGE Program for funding this research. (Project No. ECCS-1032647).

## REFERENCES

1. Adrian RJ, Christensen KT, Liu ZC. Analysis and interpretation of instantaneous turbulent velocity fields. *Experiments in Fluids* 2000; **29**(3): 275–290.
2. Berkooz G, Holmes P, Lumley JL. The proper orthogonal decomposition in the analysis of turbulent flows. *Annual Review of Fluid Mechanics* 1993; **25**(1): 539–575.
3. Borée J. Extended proper orthogonal decomposition: a tool to analyse correlated events in turbulent flows. *Experiments in Fluids* 2003; **35**(2): 188–192.
4. Kostas J, Soria J, Chong MS. A comparison between snapshot POD analysis of PIV velocity and vorticity data. *Experiments in Fluids* 2005; **38**(2): 146–160.
5. Cordier L, Bergmann M. Post-processing of experimental and numerical data. Lecture Series: von Karman Institute for Fluid Mechanics, 2003-04.
6. Bonnet JP, Cole DR, Delville J, Glauser MN, Ukeiley LS. Stochastic estimation and proper orthogonal decomposition: complementary techniques for identifying structure. *Experiments in Fluids* 1994; **17**(5): 307–314.
7. Lumley JL. *Stochastic tools in turbulence*. Dover Publications, Inc.: Mineola, New York, 2007.
8. Citriniti JH, George WK. Reconstruction of the global velocity field in the axisymmetric mixing layer utilizing the proper orthogonal decomposition. *Journal of Fluid Mechanics* 2000; **418**(2000): 137–166.
9. Tutkun M, Johansson PBV, George WK. Three-component vectorial proper orthogonal decomposition of axisymmetric wake behind a disk. *AIAA Journal* 2008/05/01; **46**(5): 1118–1134.
10. Saranyasoontorn K, Manuel L. Low-dimensional representations of inflow turbulence and wind turbine response using proper orthogonal decomposition. *ASME Journal of Solar Energy Engineering* 2005; **127**(4): 553.
11. Lumley JL. The Structure of Inhomogeneous Turbulent Flows. In *Atmospheric Turbulence and Radio Wave Propagation*, Yaglom AM, Tatarsky VI (eds) Vol. 192. Publishing House Nauka: Moscow, USSR, 1967; 166–176.
12. Pedersen JM. Analysis of planar measurements of turbulent flows, *Ph.D. Thesis*, Technical University of Denmark (DTU), Department of Mechanical Engineering, Building 403, Technical University of Denmark, DK-2800 Lyngby, Denmark, February 2003.
13. Sirovich L. Turbulence and the dynamics of coherent structures. *Quarterly of Applied Mathematics* 1987; **45**: 561–571.
14. Chamorro LP, Arndt REA, Sotiropoulos F. Reynolds number dependence of turbulence statistics in the wake of wind turbines. *Wind Energy* 2012; **15**(5): 733–742.
15. Cal RB, Lebron J, Castillo L, Kang HS, Meneveau C. Experimental study of the horizontally averaged flow structure in a model wind-turbine array boundary layer. *Journal of Renewable and Sustainable Energy* 2010; **2**(1): 013106.
16. Chamorro LP, Arndt REA, Sotiropoulos F. Turbulent flow properties around a staggered wind farm. *Boundary-Layer Meteorology* 2011; **141**(3): 349–367.
17. Chamorro LP, Porté-Agel F. Turbulent flow inside and above a wind farm: a wind-tunnel study. *Energies* 2011; **4**(11): 1916–1936.
18. Hamilton N, Kang HS, Meneveau C, Cal RB. Statistical analysis of kinetic energy entrainment in a model wind turbine array boundary layer. *Journal of Renewable and Sustainable Energy* 2012; **4**(6): 063105–063105.